JACS
JOURNAL OF THE AMERICAN CHEMICAL SOCIETY
Article
pubs.acs.org/JACS

The Origin of Capacity Fade in the Li_2MnO_3·LiMO_2 (M = Li, Ni, Co, Mn) Microsphere Positive Electrode: An *Operando* Neutron Diffraction and Transmission X-ray Microscopy Study

Chih-Jung Chen,[†,▽] Wei Kong Pang,[‡,§,▽] Tatsuhiro Mori,[†] Vanessa K. Peterson,[*,‡] Neeraj Sharma,[#] Po-Han Lee,[∥] She-huang Wu,[∥] Chun-Chieh Wang,[⊥] Yen-Fang Song,[⊥] and Ru-Shi Liu[*,†,¶]

[†]Department of Chemistry, National Taiwan University, Taipei 106, Taiwan

[‡]Australian Centre for Neutron Scattering, Australian Nuclear Science and Technology Organisation, Lucas Heights, NSW 2234, Australia

[§]Institute for Superconducting & Electronic Materials, University of Wollongong, Wollongong, NSW 2522, Australia

[#]School of Chemistry, UNSW Australia, Sydney, NSW 2052, Australia

[∥]Department of Materials Engineering, Tatung University, Taipei City 104, Taiwan

[⊥]National Synchrotron Radiation Research Center, Hsinchu 30076, Taiwan

[¶]Department of Mechanical Engineering and Graduate Institute of Manufacturing Technology, National Taipei University of Technology, Taipei 10608, Taiwan

Supporting Information

ABSTRACT: The mechanism of capacity fade of the Li_2MnO_3·LiMO_2 (M = Li, Ni, Co, Mn) composite positive electrode within a full cell was investigated using a combination of *operando* neutron powder diffraction and transmission X-ray microscopy methods, enabling the phase, crystallographic, and morphological evolution of the material during electrochemical cycling to be understood. The electrode was shown to initially consist of 73(1) wt % $R\bar{3}m$ LiMO_2 with the remaining 27(1) wt % $C2/m$ Li_2MnO_3 likely existing as an intergrowth. Cracking in the Li_2MnO_3·LiMO_2 electrode particle under *operando* microscopy observation was revealed to be initiated by the solid-solution reaction of the LiMO_2 phase on charge to 4.55 V vs Li^+/Li and intensified during further charge to 4.7 V vs Li^+/Li during the concurrent two-phase reaction of the LiMO_2 phase, involving the largest lattice change of any phase, and oxygen evolution from the Li_2MnO_3 phase. Notably, significant healing of the generated cracks in the Li_2MnO_3·LiMO_2 electrode particle occurred during subsequent lithiation on discharge, with this rehealing being principally associated with the solid-solution reaction of the LiMO_2 phase. This work reveals that while it is the reduction of lattice size of electrode phases during charge that results in cracking of the Li_2MnO_3·LiMO_2 electrode particle, with the extent of cracking correlated to the magnitude of the size change, crack healing is possible in the reverse solid-solution reaction occurring during discharge. Importantly, it is the phase separation during the two-phase reaction of the LiMO_2 phase that prevents the complete healing of the electrode particle, leading to pulverization over extended cycling. This work points to the minimization of behavior leading to phase separation, such as two-phase and oxygen evolution, as a key strategy in preventing capacity fade of the electrode.

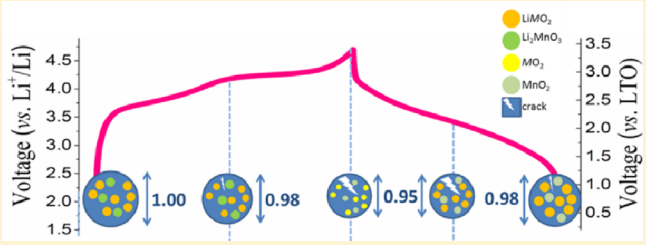

INTRODUCTION

The annual global-energy consumption of approximately 15 TW is estimated to increase to 25−27 TW by 2050.[1] In the US, ∼16.8% of annual energy consumption arises from the transportation sector,[2] the dominant fuel for which is gasoline, with such fossil fuels resulting in the emission of 30.4 Gt of carbon dioxide, implicated in climate change.[3] The development of electric vehicles may alleviate our reliance on fossil fuels, and among the energy-storage devices developed for such applications, lithium-ion batteries (LIBs) have relatively high energy density compared to other battery types and are the leading candidate.[4] The capacity of an electrode is related to both the number of lithium ions that can be reversibly inserted into it and its molecular mass. In a LIB, positive electrodes have a maximum theoretical capacity in the range 268−300 mA h g^{-1}, compared with typical negative electrodes such as graphite (372 mA h g^{-1})[5] and Si (4200 mA h g^{-1}),[6] and are thus a major performance bottleneck. Commonly used positive electrodes in LIBs are $LiCoO_2$ and substituted variants, $LiMn_2O_4$, and $LiFePO_4$. Rapid developments in advanced technologies such as electric transportation have motivated the search for novel

Received: April 16, 2016
Published: June 17, 2016

DOI: 10.1021/jacs.6b03932
J. Am. Chem. Soc. 2016, 138, 8824−8833

positive electrode materials with improved performance characteristics such as high rate capability and energy density. The working potential of layered $LiCoO_2$ is ~3.8 V, and although the theoretical capacity of this positive electrode material is 274 mA h g^{-1}, only ~50% of Li^+ ions can be reversibly extracted from its structure, as beyond this an irreversible structural transition occurs.[7] Thus, the vehicular application of $LiCoO_2$ is restricted by its low practical capacity (~140 mA h g^{-1}).[8] The spinel $LiMn_2O_4$ features a high working plateau (4.0 V), although Mn^{2+} ions, from the disassociation of Mn^{3+} to Mn^{2+} and Mn^{4+}, dissolve in the electrolyte within a battery, resulting in poor cycling performance after several charge and discharge steps.[9,10] The operating voltage and capacity of $LiFePO_4$ limit its energy density, making this material relatively unsuitable for the high-power demands of electric vehicles.[11,12]

The $xLi_2MnO_3\cdot(1-x)LiMO_2$ ($Li_{1+z}MO_2$ where M = Ni, Co Mn) system, consisting of Li_2MnO_3 (with $C2/m$ space group) and $LiMO_2$ (with $R\bar{3}m$ space group), is a promising positive electrode with a capacity of ~250−300 mA h g^{-1},[13] approaching its theoretical intercalation capacity. Despite this, this material has several drawbacks, including poor rate[14−16] and cycling performance,[14,17,18] and a large hysteresis in the charge and discharge curves, particularly in the first few cycles.[19−21] Therefore, reducing the capacity loss (50−100 mA h g^{-1}) of $Li_2MnO_3\cdot LiMO_2$ is a major focus of LIB research.[9,13]

$Li_{1.2}Mn_{0.567}Ni_{0.166}Co_{0.067}O_2$ is shown to exist predominantly as a bulk $LiMO_2$ structure with an intergrowth of a Li_2MnO_3-like phase, with these phases heterointerface in particle grains.[22] The Li_2MnO_3 phase is shown to exhibit reflections unindexed by the $C2/m$ space group, with these attributed to stacking faults of the ordered lithium/manganese layers along the c-axis.[23]

Understanding the atomistic and molecular-scale origin of battery performance is key to improving the capacity and cycling performance of electrode materials. Most layered-oxide positive electrodes, such as $LiCoO_2$[7] and $Li(Ni_{1/3}Mn_{1/3}Co_{1/3})O_2$,[24] undergo a predominantly solid-solution reaction within their normal operational voltage window, although a two-phase reaction during overdelithiation may present at higher voltages. Charging beyond the normal operating range in order to increase energy density and capacity, e.g., 4.5 or 4.8 V vs Li^+/Li for the $LiCoO_2$ material, results in a two-phase reaction that is similar to that occurring in spinel-type materials such as $LiMn_2O_4$.[25,26] The coexistence of multiple phases over a wide range of lithium content results in phase bordering and interface movement through material grains, and maintaining structure type during lithiation may avoid such phase-border shifts and result in better cycle life.[27]

For the $Li_2MnO_3\cdot LiMO_2$ composite electrode, the working window is 2.0−4.8 V vs Li^+/Li.[9,23,28] The $Li_{1.2}Mn_{0.54}Ni_{0.13}Co_{0.13}O_2$ material exhibits significant capacity loss beyond 3.5 V, which is attributed to the transformation from the layered Li_2MnO_3 to a nanodomained spinel-like $LiMn_2O_4$ phase.[29] Phase transitions of the $xLi_2MnO_3\cdot(1-x)LiMO_2$ composite electrode during charge and discharge below 4.4 V (vs Li^+/Li)[9] are reported to involve predominantly the $LiMO_2$ component, which oxidizes to Li_xMO_2 where $x \sim 0$ as Li^+ ions are extracted during charge to 4.4 V (vs Li^+/Li). During discharge, MO_2 reversibly reduces to $LiMO_2$ as Li^+ ions are reinserted. During this process the Li_2MnO_3 phase is inactive as Mn^{4+} ions cannot oxidize further. Instead, the Li_2MnO_3 phase is reported to function as a buffer, preventing the structural decomposition of $LiMO_2$ during the extraction of lithium ions.[9,13] On charge beyond 4.4 V (vs Li^+/Li), Li_2MnO_3 undergoes an irreversible oxygen-evolution reaction, resulting in the removal of 2 Li^+ and O^{2-} (a total loss of Li_2O) and the formation of the electrochemically active MnO_2-like phase.[13] During discharge, Li^+ is only partially reinserted into the MnO_2-like phase, resulting in an initial and irreversible capacity loss in the first cycle.[9,13] Thackeray et al. considered the $Li_2MnO_3\cdot LiMO_2$ as a rock-salt type structure where the octahedral sites of the cubic close-packed oxygen array are occupied, with this phase transforming into a quasi-spinel-like type structure during electrochemical cycling. Under this scheme, capacity fade is thought to originate as a result of the dissolution of Mn^{2+} in a similar manner to that occurring in the $LiMn_2O_4$ positive electrode.[9]

Members of the $xLi_2MnO_3\cdot(1-x)LiMO_2$ family have been investigated using in situ and *operando* X-ray diffraction (XRD). Mohanty et al. reported the structural transformations of the $Li_{1.2}Co_{0.1}Mn_{0.55}Ni_{0.15}O_2$ ($Li(Li_{0.2}Co_{0.1}Mn_{0.55}Ni_{0.15})O_2$) electrode. Ex-situ XRD and selected-area electron diffraction (SAED) data show the as-prepared material to be a combination of $R\bar{3}m$ and $C2/m$ phases, appearing as a intergrown system.[30] In their *operando* XRD data, Mohanty et al. are unable to observe the Li_2MnO_3 $C2/m$ phase and describe the material as a single $R\bar{3}m$ phase with some Li^+ occupying the 3*b* (Li) and 3*a* (transition metal) crystallographic sites, alongside Ni also occupying the 3*b* site. On charge to 4.4 V (vs Li^+/Li), the c lattice parameter of the $R\bar{3}m$ phase increased while the a lattice parameter reduced. The increase in the c lattice parameter arises as a result of enhanced electrostatic repulsion between the O layers, while the reduction in the a lattice parameter occurs as a result of the increased oxidation state of M ions as Li^+ is extracted. On further charging to 4.8 V, the migration of M ions to the Li^+ layer causes the c lattice parameter to decrease as further Li^+ is extracted, while the a lattice parameter remains unchanged, as a result of the stable oxidation state of the M transition metals during the evolution of oxygen. This behavior is reversible on discharge. Shen et al. investigated the $0.5Li_2MnO_3\cdot 0.5LiNi_{0.292}Co_{0.375}Mn_{0.333}O_2$ material, and used XRD and SAED to show the as-synthesized material to be a combination of $R\bar{3}m$ $LiMO_2$ and Li_2MnO_3 $C2/m$ structured phases.[31] In their multipotential profile XRD data, they model this material as a single $R\bar{3}m$ phase as per Mohanty et al. Shen et al. report a lattice parameter evolution with battery state of charge that differs to that of Mohanty et al. Compared with the expansion of the c lattice parameter and reduction of the a lattice parameter on charge reported by Mohanty et al., Shen et al. observed the c lattice parameter to decrease and the a lattice parameter to remain unchanged. Shen et al., attribute this behavior to the absence of oxidation during the delithiation occurring alongside the migration of Ni^{2+} from the transition-metal site to the Li^+ site, on charge from 3.7 to 4.3 V. These differences likely arise from differences in electrochemical steps used in their multipotential approach. Liu et al.[32] studied the $Li_1(Li_{0.2}Ni_{0.15}Mn_{0.55}Co_{0.1})O_2$ material and do not report characterization results for the as-prepared compound. In their *operando* NPD they model the material as a single $R\bar{3}m$ phase as per Mohanty et al.[30] and Shen et al.[31] On charge to 4.3 V (vs Li^+/Li) the c lattice parameter increased while the a lattice parameter reduced as consistent with results of Mohanty et al.,[30] corresponding to the extraction of lithium from the 3*b* site. Beyond 4.4 V (vs Li^+/Li) the c lattice parameter decreased

DOI: 10.1021/jacs.6b03932
J. Am. Chem. Soc. 2016, 138, 8824−8833

while the *a* lattice parameter remained unchanged. During the plateau at 4.4 V (vs Li^+/Li) they report lithium extraction from both 3*b* and 3*a* sites and a ~30% reduction in lithium content of the 3*a* site after the first cycle.

In the present study we investigate the structural evolution of the $Li_2MnO_3{\cdot}LiMO_2$ positive electrode with a high charge capacity (302 mA h g^{-1}) using *operando* neutron powder diffraction (NPD) within a full cell containing a LTO negative electrode. This information is combined, for the first time, with morphology measurements of the $Li_2MnO_3{\cdot}LiMO_2$ positive electrode that are obtained using *operando* transmission X-ray microscopy (TXM), allowing the correlation of atomic-scale crystallographic and morphological detail to understand electrode function. This combination revealed in detail the underlying phase transformations and mechanisms that are responsible for the initiation and intensification of particle cracking that likely leads to pulverization and capacity fade in this electrode.

EXPERIMENTAL SECTION

Preparation of Electrode Materials. $Li_2MnO_3{\cdot}LiMO_2$ was prepared by a coprecipitation method. $MnSO_4{\cdot}H_2O$ (JT Baker, 98–101%), $NiSO_4{\cdot}6H_2O$ (JT Baker, 98–102%), and $CoSO_4{\cdot}7H_2O$ (Alfa Aesar, 98%) were dissolved in 300 mL deionized (DI) water as a precursor solution. 300 mL of 1 M Na_2CO_3 (Sigma-Aldrich, 99.8%) was added into a round-bottom flask and stirred at 500 rpm and CO_2 gas was purged through the solution until the pH was 5.5. NH_4OH (Sigma-Aldrich, 30–33%) was then added dropwise into the DI water until the acidity reached pH 7.5–8. The precursor solution was then gradually dropped into this solution, and then the remaining precursor and Na_2CO_3 solutions were simultaneously added, during which the pH was maintained at 7.5–8 by further purging with CO_2 gas and NH_4OH addition. The combined solution was stirred for 24 h, filtered, and the precipitate washed with DI water and then dried. The dried powder was ground with Li_2CO_3 (Alfa Aesar, 99.998%) and heated at 900 °C in air for 12 h before quenching on a copper plate to obtain $Li_2MnO_3{\cdot}LiMO_2$.

Hydrous titanium oxide was prepared by the hydrolysis of titanium tetraisopropoxide (TTIP, 97%, Aldrich) as the precursor for synthesizing $Li_4Ti_5O_{12}$ (LTO). Potassium chloride (KCl) (JT Baker, 100%) was dissolved in DI water to prepare a 0.1 M aqueous solution. This solution (0.4 mL) was mixed with 100 mL ethanol and 2.2 mL TTIP, and stirred for 10 min and placed in air atmosphere for 24 h. The resultant precipitate was collected as hydrous titanium oxide. LTO was prepared by dissolving LiOH (Aldrich, > 98%, 3 mmol) in a 100 mL solution of ethanol and DI water (volume ratio 1:1) and dispersing into this 1.2 g hydrous titanium oxide and vigorously stirring for 15 min. The suspension was transferred to a 100 mL Teflon-lined stainless steel autoclave and heated at 180 °C for 12 h. The resulting powder was collected by vacuum filtration, washed with DI water several times, and dried at 180 °C for 3 h followed by a heat treatment at 500 °C in air for 1 h to obtain the final LTO.

Characterization of As-Synthesized Electrode Materials. Morphological examination of the as-synthesized $Li_2MnO_3{\cdot}LiMO_2$ and LTO electrode materials was performed using scanning electron microscopy (SEM) with a JEOL JSM-6700F field-emission instrument. The electrode materials were also characterized using X-ray diffraction (XRD) with a Bruker D2 Phaser with CuKα radiation (λ = 1.54178 Å). The crystal structure of the $Li_2MnO_3{\cdot}LiMO_2$ was determined by performing Rietveld analysis against these XRD and high-resolution NPD data collected using ECHIDNA,[33] the high-resolution neutron powder diffractometer at the Open Pool Australian Light-water (OPAL) research reactor, at the Australian Nuclear Science and Technology Organisation (ANSTO). The wavelength of neutrons were 1.6215(1) and 2.4393(2) Å, determined using the $La^{11}B_6$ NIST standard reference material (SRM) 660b. The NPD data were obtained in 2.75–163.95° in 2θ with a step size of 0.125°. GSAS-II[34] was employed to perform joint Rietveld analysis of the XRD and the two high-resolution NPD data sets. The refineable parameters included background coefficients, zero, peak shape parameters, lattice parameters, phase scale, atomic position parameters, site occupancy factors (SOF), and isotropic atomic displacement parameters (U_{iso}). Inductively coupled plasma mass-spectrometry (ICP-MS) was also performed using an Agilent 7700e to determine the Li: Ni: Mn: Co ratio in the $Li_2MnO_3{\cdot}LiMO_2$ material.

Electrochemical Characterization of Materials. The electrochemical performance of the electrode materials were determined using coin cell-type batteries and a battery tester (AcuTech Systems Co., Ltd.). Electrodes for coin cell batteries were prepared by stirring vigorously overnight the active material, super-P (carbon black), and polyvinylidene fluoride (PVDF) binder, in a weight ratio 8:1:1, in *N*-methylpyrrolidinone (NMP) and doctor-blading the resultant slurry onto Al foil, before drying overnight at 70 °C in vacuum. Coin-type cells were assembled in an argon-filled glovebox (O_2 and H_2O < 1 ppm). The counter electrode was Li foil and the electrolyte was $LiPF_6$ (1 M) dissolved in a mixture of ethylene carbonate (EC) and dimethyl carbonate (DMC) (1:1 volume ratio). The assembled coin cells were tested using cyclic voltammetry (CV) at a scan rate of 0.5 mV s^{-1}. The capacity and cycling performance of $Li_2MnO_3{\cdot}LiMO_2$ was measured at a current density of 10 mA g^{-1} within a voltage window of 2.0–4.8 V (vs Li^+/Li). The electrochemical performance of the LTO electrode was also tested in a coin-type cell at a current density of 20 mA g^{-1} within a voltage window of 1.0–3.0 V (vs Li^+/Li).

***Operando* Neutron Powder Diffraction.** A customized pouch-type battery was prepared for *operando* neutron powder diffraction (NPD) analysis as per the method reported in Pang and Peterson,[35] using the as-synthesized $Li_2MnO_3{\cdot}LiMO_2$ and LTO electrode powders, and the cell filled with deuterated EC: DMC (1:1 in vol) electrolyte. Lithium is highly neutron absorbing and the relatively large amount required for the neutron friendly battery can interplay unfavorably with the sample geometry, as well as potentially resulting in lithium plating. Therefore, the well-established and reliable zero-strain LTO electrode was chosen as the counter electrode for the NPD battery, where the solid-electrolyte interface layer formation and Li metal deposition on the LTO surface, leading to degradation of the LIB, is avoided. During the *operando* NPD experiment the pouch-type battery was cycled galvanostatically using a postentiostat/galvanostat (Autolab PG302N) at a current of 11.6 mA (~0.1 C) with a constant voltage step at 3.4 V in the first cycle and 3.5 V in the second cycle (vs LTO). *Operando* NPD data were collected using WOMBAT,[36] the high-intensity neutron powder diffractometer at ANSTO. A neutron beam of wavelength of 2.95405(2) Å was used, determined using Al_2O_3 SRM 676. The data were continuously obtained with a collection time of 10 min per pattern in the 2θ range 16.0–136.9°. FullProf with visualization in WinPLOTR[37,38] was used to perform sequential Rietveld refinements using the *operando* NPD data in the 2θ range of 60–130°. The Large Array Manipulation Program (LAMP)[39] was employed to perform single-peak analyses of the $LiMO_2$ 012 and LTO 222 reflections.

***Operando* Transmission X-ray Microscopy.** A coin cell for *operando* transmission X-ray microscopy (TXM) measurement was made using an electrode slurry prepared by stirring vigorously overnight the active material, super-P, and PVDF binder in a weight ratio 8:1:1, in NMP. A free-standing electrode was prepared as per other work[40−43] by coating the slurry of the active material onto a Cu foil and then etching by immersion in a $FeCl_3$ aqueous solution. The obtained free-standing electrode was subsequently rinsed with DI water, dried at 80 °C, and used in a coin cell with open windows (Figure S1). The free-standing electrode was adhered to the top cap of the modified coin cell, which then functioned as the current collector. TXM data were obtained at the 01B1 beamline of the National Synchrotron Radiation Research Center (NSRRC) in Hsinchu City, Taiwan (Figure S1c). Synchrotron X-rays with an energy of 8 keV were used and the transmitted beam passed through a zone-plate and a phase ring to generate an image. The phase ring was positioned at the back focal plane of the zone plate which recorded phase-contrast images at the charge-coupled device (CCD) detector. The spatial

DOI: 10.1021/jacs.6b03932
J. Am. Chem. Soc. 2016, 138, 8824−8833

resolution and field of view of TXM is 50 nm and 15 × 15 μm^2, respectively. The electrochemical characterization was simultaneously carried out using a battery tester (AcuTech Systems Co., Ltd.). The collected TXM images were further processed and analyzed using ImageJ.

RESULTS AND DISCUSSION

Joint structural refinement of the as-synthesized Li_2MnO_3·$LiMO_2$ using the two NPD and one XRD data sets (Figure 1, Tables 1 and 2) indicate Li_2MnO_3 and $LiMO_2$ components comprising 27(1) and 73(1) wt % (21(1) and 79(1) mol %), respectively. As expected, the Li_2MnO_3 component was well described by a monoclinic structure with $C2/m$ space group,[30]

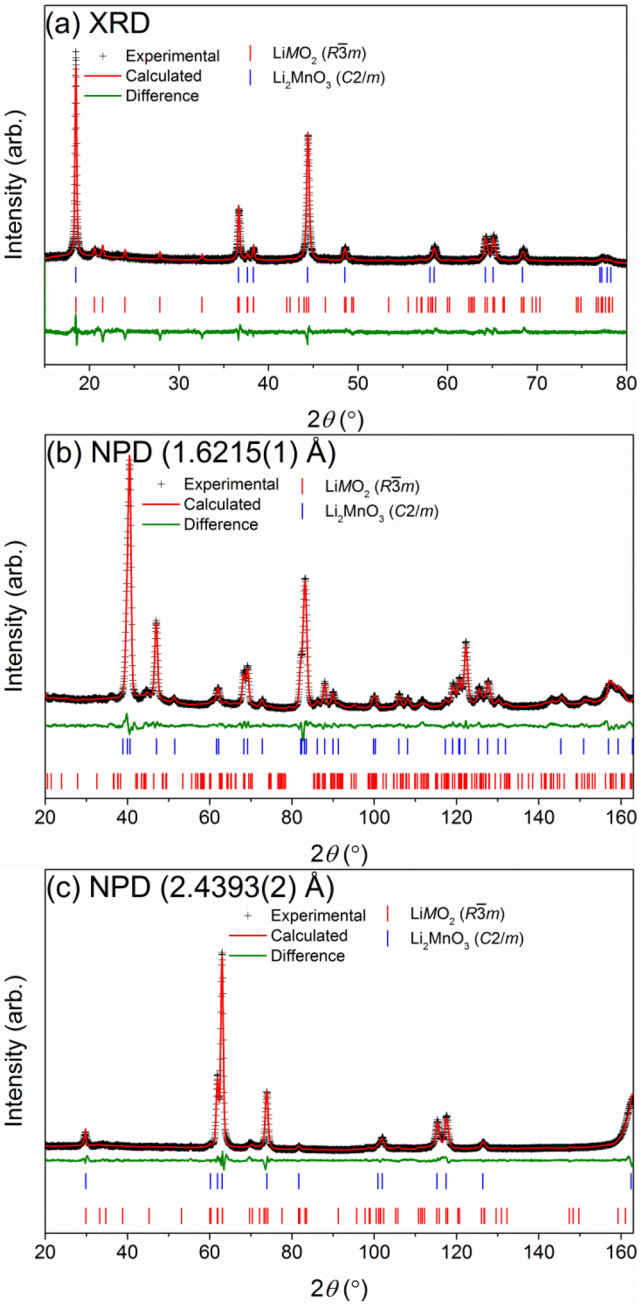

Figure 1. Rietveld-refinement profiles for the Li_2MnO_3·$LiMO_2$ material using (a) XRD data at 1.54178 Å, (b) NPD data at λ = 1.6215(1), and (c) NPD data at λ = 2.4393(2)) Å, with corresponding weighted profile R-factors (R_{wp}) of 2.73, 4.43, and 3.86%, respectively.

Table 1. Crystallographic Details of the Li_2MnO_3 Phase Obtained from Joint Rietveld Analysis Using XRD and Two NPD Data Sets

Li_2MnO_3 (space group = $C2/m$) a = 4.952(2) Å, b = 8.562(1) Å, c = 5.037(2) Å, β = 109.42(2)°

atom	site	x	y	z	U_{iso} (Å^2)	SOF
Li	2b	0	1/2	0	0.01	1
Li	2c	0	0	1/2	0.01	1
Li	4h	0	0.683(2)	1/2	0.01	1
Mn	4g	0	0.184(1)	0	0.05(1)	1
O	4i	0.174(3)	0	0.232(2)	0.08(1)	1
O	8j	0.261(1)	0.341(1)	0.225(1)	0.02(1)	1

Table 2. Crystallographic Details of the $LiMO_2$ Phase Obtained from Joint Rietveld Analysis Using XRD and Two NPD Data Sets

$Li_{0.959}Ni_{0.041}(Li_{0.245}Ni_{0.206}Mn_{0.433}Co_{0.116})O_2$ (space group = $R\bar{3}m$) a = b = 2.8583(2) Å, c = 14.2545(5) Å

atom	site	x	y	z	U_{iso} (Å^2)	SOF
Li	3b	0	0	1/2	0.013(1)[b]	0.959(2)[a]
Ni	3b	0	0	1/2	0.013(1)[b]	0.041(2)[a]
Li	3a	0	0	0	0.01	0.245[a]
Ni	3a	0	0	0	0.01	0.206[a]
Mn	3a	0	0	0	0.01	0.433[a]
Co	3a	0	0	0	0.01	0.116[a]
O	6c	0	0	0.2584(1)	0.014(1)	1

[a]Constrained to sum to unity. [b]Constrained to be same.

and $LiMO_2$ was found to adopt an α-$NaFeO_2$ structure with an $R\bar{3}m$ space group.[44] The ratios of Li:Mn:Ni:Co determined using ICP-MS were found to be 1.0(56):0.407(9):0.138(4):0.0828(1). The two phase nature of this electrode is consistent with previous work demonstrating that bulk $LiMO_2$ presents as particles intergrown with a Li_2MnO_3 phase.[22] The LTO material was examined using XRD (Figure S2) and confirmed to be phase pure with $Fd\bar{3}m$ space-group symmetry.

SEM analysis of Li_2MnO_3·$LiMO_2$ reveals a spherical morphology featuring pinholes on the surface, with a secondary particle size of ∼5−20 μm (Figure 2a). Such pinholes are thought to increase surface area and enhance the diffusion of Li^+ into the particle core, improving electrochemical performance.[45] The primary particle size of the Li_2MnO_3·$LiMO_2$ was found to be ∼39 nm, obtained from the Scherrer equation using the strongest peak in the XRD data. Similarly, SEM analysis of LTO also revealed particles with a spherical morphology, being composed of primary particles with diameter 20−30 nm.

The charge and discharge curves of a coin cell containing Li_2MnO_3·$LiMO_2$ at a current density of 10 mA g^{-1} are shown in Figure 3a. The first specific charge and discharge capacities were 302 and 238 mA h g^{-1}, respectively. This initial capacity loss is attributed to the irreversible activation of Li_2MnO_3,[46] leading to the low initial Coulombic efficiency of ∼79%. In the second cycle, the specific charge capacity reduces to 241 mA h g^{-1}, ∼79.8% of the initial capacity, and the Coulombic efficiency increases to ∼94.2%. The 10th specific charge capacity is ∼69.5% (210 mAh g^{-1}) of the initial value, and by the 80th cycle capacity retention is ∼38.6% (Figure 3b). Despite this relatively good capacity, the capacity fade of Li_2MnO_3·$LiMO_2$ needs to be addressed. The charge and

DOI: 10.1021/jacs.6b03932
J. Am. Chem. Soc. 2016, 138, 8824−8833

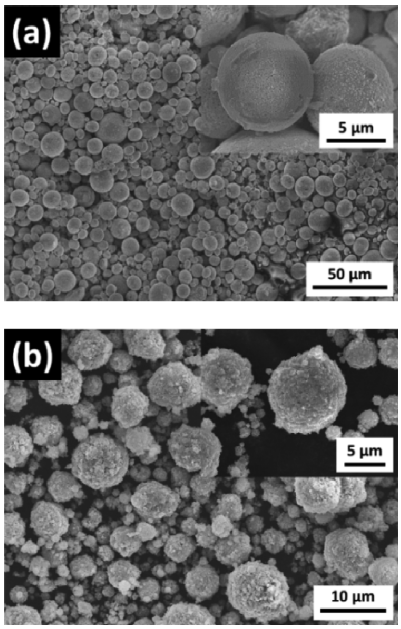

Figure 2. SEM images of (a) $Li_2MnO_3{\cdot}LiMO_2$ and (b) LTO.

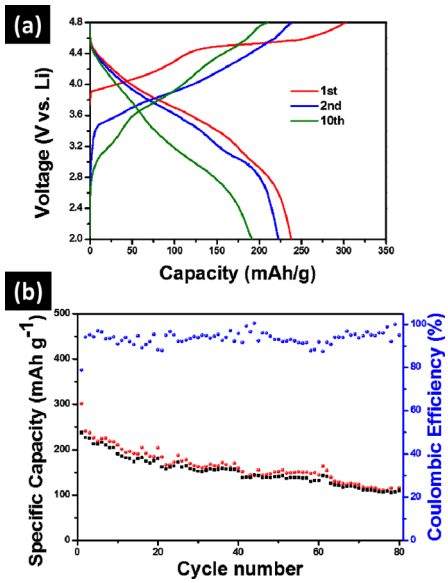

Figure 3. (a) The charge and discharge curves of a coin cell containing $Li_2MnO_3{\cdot}LiMO_2$ during the 1st, 2nd, and 10th cycles. (b) The corresponding cycle performance and Coulombic efficiency of this cell at a current density of 10 mA g^{-1}.

discharge curve of a coin cell containing LTO at 20 mA g^{-1} is shown in Figure S3a. The first discharge and charge capacities of LTO were 173 and 162 mA h g^{-1}, respectively, and the initial Coulombic efficiency was 93.7%. The LTO discharge and charge plateaus were ~1.54 and 1.58 V, respectively. Coulombic efficiencies in the following cycles (up to 80) were retained at ~100%. The discharge and charge plateaus were stable during subsequent measurements, indicating that LTO is robust to performance degradation. The 80th discharge capacity of LTO was ~153 mA h g^{-1}, indicating 88.4% retention of initial capacity (Figure S3b).

Figure S4 shows the CV results using coin cells with $Li_2MnO_3{\cdot}LiMO_2$ as the working electrode. A broad anodic peak is observed in the first charge, from ~3.7 to 4.4 V (vs Li^+/Li), that is associated with the oxidation of Ni^{2+} and Co^{3+} in $LiMO_2$ to Ni^{4+} and Co^{4+}.[47] At higher potential, a second anodic peak (>4.5 V (vs Li^+/Li)) appears as a result of the activation of Li_2MnO_3, involving the simultaneous extraction of Li^+ and evolution of oxygen.[48]

During the first discharge, a broad cathodic peak at ~3.6 V is observed, arising from the reduction of Ni^{4+} and Co^{4+} in $LiMO_2$, and a second cathodic peak appears at ~3.0 V, arising from the reduction of Mn^{4+}.[49] In subsequent cycles, the first anodic peak broadens and shifts to ~4.2 V (vs Li^+/Li), and the second anodic peak gradually disappears, indicating irreversibility of the reaction involving Li^+ extraction and oxygen evolution from Li_2MnO_3.[46] Finally, the cathodic peak arising from the reduction of Mn^{4+} shifts to lower potential (~2.8 V (vs Li^+/Li)).

Operando NPD was used to investigate the $Li_2MnO_3{\cdot}LiMO_2$ phase and structure evolution in a full cell containing a LTO negative electrode during cycling between 0.5 and 3.5 V (vs LTO). The charge and discharge curve of this battery during the *operando* NPD experiment is shown in Figure S5.

The *operando* NPD patterns of the $Li_2MnO_3{\cdot}LiMO_2$||LTO full battery (Figure 4, showing NPD data as a contour plot

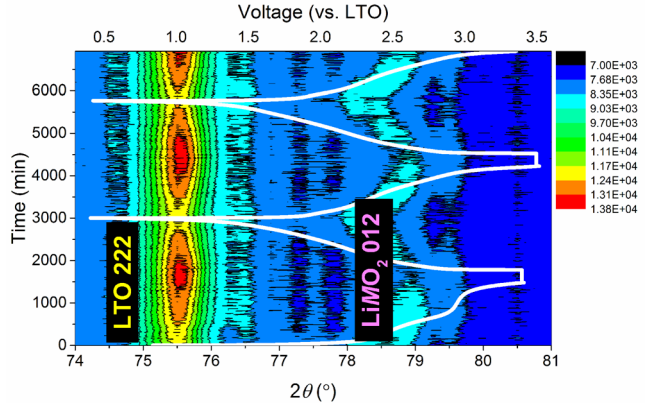

Figure 4. (a) Contour plot of *operando* NPD data for the $Li_2MnO_3{\cdot}LiMO_2$||LTO battery, with intensity (arb.) shown in color with the scale on the right. Voltage is shown in white.

against time in a selected 2θ range) reveal changes that correspond to the phase evolution of the electrodes in the battery during electrochemical cycling. The charge−discharge curve for this battery has features that are near-identical to that obtained for coin cells containing Li as the counter electrode. Each NPD pattern within the *operando* series is for the structural average over the 10 min collection time. The Rietveld-refinement plot using the first pattern in the *operando* data set is shown in Figure S6, with the $LiMO_2$ and LTO electrode phases, as well as the Al and Cu current collectors, observable. The Li_2MnO_3 component of the positive electrode, as well as Li_2CO_3, Li_2O, and $LiOH{\cdot}H_2O$ phases expected to be generated at particular potentials,[48] were not observable in these data, presumably as a result of the relatively lower symmetry and smaller amount of these phases, in conjunction with the significant background contribution from the H-containing battery components. During the sequential Rietveld refinement, the ratio of these phases remained nearly unchanged, and the phase scale factors were subsequently fixed during the sequential refinement. The goodness of fit (χ^2) of each Rietveld refinement during sequential analysis is given

DOI: 10.1021/jacs.6b03932
J. Am. Chem. Soc. 2016, 138, 8824−8833

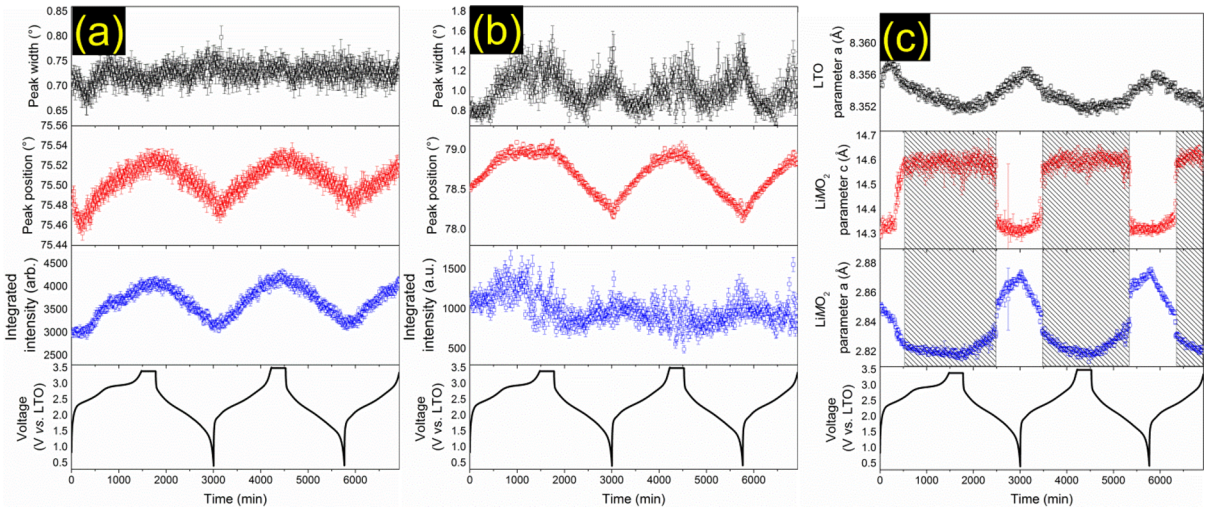

Figure 5. Results of the analysis of the *operando* NPD data for the Li_2MnO_3·$LiMO_2$||LTO battery, observing only the $LiMO_2$ and LTO phases of the electrode with $R\bar{3}m$ and $Fd\bar{3}m$ space-group symmetry, respectively. Single-peak fitting results for (a) the LTO 222 and (b) $LiMO_2$ 012 reflections, including the peak width, position, and (integrated) intensity. (c) LTO and $LiMO_2$ lattice parameter obtained from the sequential Rietveld analysis.

in Figure S7. The Rietveld analysis results are supported by single peak-fitting analysis of the strongest diffraction peaks from the LTO and $LiMO_2$ phases in the *operando* NPD data, at 2θ of ~75.5° and 78.5°, corresponding to the LTO 222 and $LiMO_2$ 012 reflections, respectively (Figure 4, 5a, and 5b).

During battery charge to 3.0 V vs LTO (equivalent to 4.55 V vs Li^+/Li), the $LiMO_2$ *c* lattice parameter increases while the *a* lattice parameter decreases (Figure 5c). This arises because of the extraction of Li^+, leading to enhanced electrostatic repulsion between the oxygen layers, and consequential expansion along the *c*-axis, revealing delithiation via a solid-solution reaction. The contraction of the *a* lattice parameter is attributed to the oxidation of *M* ions as required for charge compensation. The lattice behavior up to 3.0 V vs LTO is similar to that reported in the *operando* studies by Mohanty et al.[30] and Liu et al.[32] Notably, the monotonic increase and decrease in *c* and *a* parameters are atypical of lithium-ion battery positive electrodes with $R\bar{3}m$ space-group symmetry,[24,50,51] but similar to that expected for the composite cathode with Li_2MnO_3 as a second phase.[13,52] Quantitatively, the $LiMO_2$ *a* lattice parameter reduces by 1.3(1)% and the *c* lattice parameter expands by 2.0(1)%. Within experimental error, the $LiMO_2$ *a* and *c* lattice parameter remain unchanged at potentials higher than 3.0 V (vs LTO or ~4.55 V vs Li^+/Li), consistent with previous *operando* results,[30,32] indicative of a two-phase reaction. During discharge, the reverse occurs, with the *a* lattice parameter expanding by 2.1(1)% and the *c* lattice parameter reducing by 2.0(1)%.

To further explore the $LiMO_2$ phase behavior, single peak fitting of the $LiMO_2$ 012 reflection was performed (Figure 5b). The extracted peak shifts are consistent with the lattice parameter behavior observed using sequential Rietveld analysis. The integrated intensity of the peak describing the $LiMO_2$ 012 reflection remains unchanged within error above 3.0 V, however, error in both the integrated intensity and width of this peak increase significantly during this process. This is consistent with the two-phase reaction of $LiMO_2$ occurring alongside the plateau at >3.1 V vs LTO (equivalent to 4.65 V vs Li^+/Li), attributed to the electrochemical activation of Li_2MnO_3 involving oxygen evolution,[9,13] with the Li_2MnO_3 phase not being considered in the work of Liu et al.[32] During its two-phase reaction, $LiMO_2$ likely evolves to a Li-poor Li_zMO_2 ($z \sim 0$) phase as similar to the evolution of CoO_2 from overdelithiated $LiCoO_2$;[7] however, the limited Q-range of the data make it impossible to determine further the details of this Li-poor phase.

It is notable that both two-phase and solid-solution reactions of the positive electrode in the battery are highly reversible, in contrast to the irreversible two-phase reaction between $LiCoO_2$ and CoO_2, explaining the good cycle performance of this electrode.[7] The LTO lattice behaved as expected, first expanding and then contracting during lithiation (Figure 5c), increasing to 8.358(1) Å after 200 min of charge followed by a reduction to 8.352(1) Å at 1500 min at 3.4 V (vs LTO), in a similar way to previously observed.[53,54] On discharge, the LTO lattice parameter linearly increased to 8.356(1) Å at 3000 min during delithiation. Overall, the 0.07(2)% change of the LTO lattice volume indicates a near zero-strain insertion behavior, with high reversibility. The changing Li^+ concentration at specific crystallographic sites influences peak position and intensity. Rietveld analysis of the *operando* NPD data revealed that during battery cycling the concentration of Li^+ at the 8*a*-site in the LTO phase remained unchanged within error, while the concentration of Li at the 16*c*-site varied (Figure S8). The peak width, position, and integrated intensity of the LTO 222 reflection during charge−discharge cycling, obtained from single-peak fitting, are shown in Figure 5a. During the first battery charge from OCV to 2.5 V vs LTO, the LTO 222 reflection intensity remained nearly unchanged while its position shifted to lower 2θ, indicating expansion. This response was followed by a monotonic increase in the reflection intensity alongside a shift in position to higher 2θ, indicating contraction, which continued until the end of lithiation (Figure 5a), consistent with Li^+ diffusion between the 8*a* and 16*c* sites occurring via the 32*e* site, as previously observed.[53−55]

Operando TXM images of a Li_2MnO_3·$LiMO_2$ particle surrounded by super-P (carbon black for improved electric conductivity) within a coin cell are shown alongside the corresponding charge and discharge curve in Figure 6 (vs Li^+/Li). The electrode material was stable under this characterization using 8 keV X-rays, as expected from previous TXM studies on similar electrodes at these energies.[56,57] The features

DOI: 10.1021/jacs.6b03932
J. Am. Chem. Soc. 2016, 138, 8824−8833

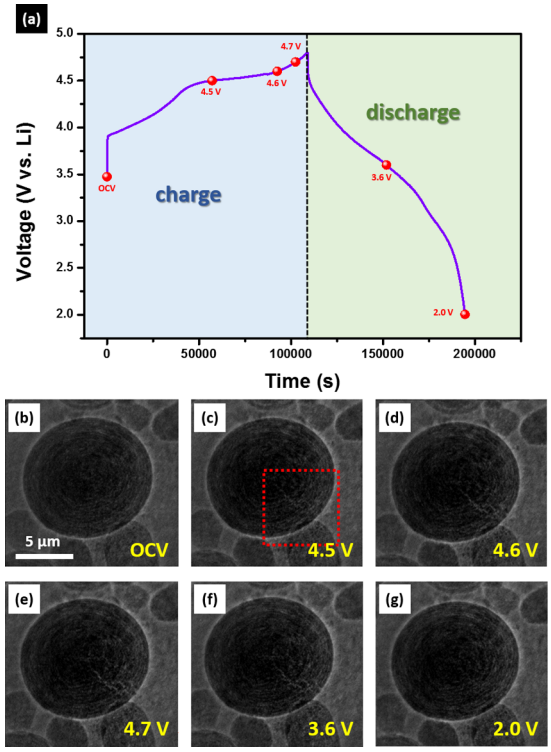

Figure 6. Charge and discharge curve of the $Li_2MnO_3{\cdot}LiMO_2$ containing battery (a) during *operando* TXM of a $Li_2MnO_3{\cdot}LiMO_2$ particle at (b) OCV, after charge to (c) 4.5 V, charge to (d) 4.6 V and (e) 4.7 V, and discharge to (f) 3.6 V and (g) 2.0 V vs Li^+/Li.

of the charge−discharge curve of this coin cell are near-identical to that of the pouch cell containing LTO used in the NPD study. The diameter of the approximately spherical $Li_2MnO_3{\cdot}LiMO_2$ particle at the open-circuit voltage (OCV) was ∼10 μm (Figure 6b). During charge to 4.5 V cracks in the $Li_2MnO_3{\cdot}LiMO_2$ electrode particle appeared (red dotted box in Figure 6c), which developed further during charge to 4.7 V (Figure 6d and 6e). During discharge, the particle cracking faded (Figure 6f), and the particle appeared to almost heal and be slightly smaller than its initial state, by 2.0 V (Figure 6g).

The change in size of the $Li_2MnO_3{\cdot}LiMO_2$ particle during charge and discharge is quantified in Table 3 and the change in

Table 3. Change in Volume of the $Li_2MnO_3{\cdot}LiMO_2$ Particle under TXM Observation

state	Figure	average diameter (μm)	vol[a] (μm³)	vol change[b] (%)
OCV	6b	10.95(1)	1278.88(3)	0
4.5 V−OCV	7a	10.78(1)	1253.16(3)	−2.011(1)
4.7−4.5 V	7b	10.66(1)	1212.74(3)	−3.226(1)
3.6−4.7 V	7c	10.66(1)	1212.74(3)	0
2.0−3.6 V	7d	10.78(1)	1253.16(3)	+3.333(1)

[a]Assuming a sphere. [b]Since previous image.

the particle appearance is shown by the differential TXM images in Figure 7. There is a strong correlation between the change in the $Li_2MnO_3{\cdot}LiMO_2$ electrode particle cracking and particle volume. The appearance of cracks in the $Li_2MnO_3{\cdot}LiMO_2$ electrode particle on charge to 4.5 V (vs Li^+/Li, red circle in Figure 7a) is accompanied by a ∼2% reduction in volume (Table 3). The significant development of the particle

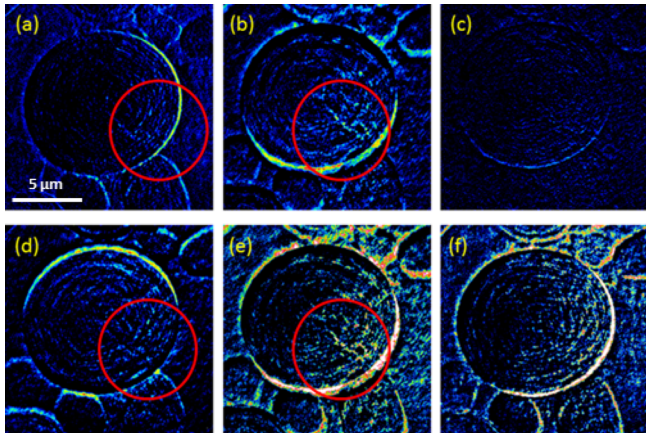

Figure 7. Differential TXM images taken between (a) 4.5 V and OCV, (b) 4.7 and 4.5 V, (c) 3.6 and 4.7 V, (d) 2.0 and 3.6 V, (e) 4.7 V and OCV, and (f) 2.0 V and OCV. Voltage is vs Li^+/Li.

cracks on charging to 4.7 V is accompanied by a more significant (∼3%) reduction in particle volume (Figure 7b). Almost no change in the particle cracks or the particle volume occurred during the discharge to 3.6 V (Figure 7c). Interestingly, further discharge to 2.0 V revealed partial healing of the cracks in the $Li_2MnO_3{\cdot}LiMO_2$ electrode, accompanied by a ∼3% volume expansion (Figure 7d). The particle crack formation and healing taking place overall on charge and discharge are shown in Figure 7e and 7f, respectively.

Electrochemical function alongside crystallographic and morphological changes of the $Li_2MnO_3{\cdot}LiMO_2$ electrode during charge and discharge are summarized in Scheme 1. During the development of the cracks in the $Li_2MnO_3{\cdot}LiMO_2$ composite particle under TXM observation on charge to 4.4 V (vs Li^+/Li), the NPD data revealed that the $LiMO_2$ phase underwent a solid-solution reaction with a ∼2.0% expansion of the *c* lattice parameter and a concomitant contraction of the *a* lattice parameter by ∼1.3%, constituting an overall volume reduction of ∼0.4%. The TXM images reveal a ∼2% volume reduction in the $Li_2MnO_3{\cdot}LiMO_2$ particle during this time.

The further crack development and volume reduction (∼3%) of the $Li_2MnO_3{\cdot}LiMO_2$ electrode particle during charging beyond 4.5 V (vs Li^+/Li) corresponds to the irreversible evolution of oxygen from the Li_2MnO_3 phase as it transforms to MnO_2 and the two-phase reaction of $LiMO_2$ revealed by the NPD data. It is the stress induced as a result of the mismatch of lattice parameters during the two-phase reaction of such electrode materials, e.g., $LiMn_2O_4$, that is thought to be responsible for capacity fade.[58] The limited Q-range of the *operando* NPD data makes it impossible to determine the product of the two-phase reaction of $LiMO_2$. Structural detail regarding this two-phase reaction was gained from examination of the $LiMO_2$ 012 reflection and previous work regarding the solid-solution and two-phase reactions of the isostructural $LiCoO_2$ material reported in Amatucci et al.[7] In the two-phase regime occurring during charge, the $LiMO_2$ d_{012} contracts by ∼0.6%, significantly less than the ∼1.1% contraction of the $LiCoO_2$ d_{012} that corresponds to a 8.1% reduction in $LiCoO_2$ lattice volume upon full delithiation. This suggests that the reduction in the $LiMO_2$ lattice during the two-phase reaction occurring on charge is likely to be less than 8% (estimated at ∼4.4% from the relative changes in d_{012} between the $LiMO_2$ and $LiCoO_2$ materials), with this constituting the most

DOI: 10.1021/jacs.6b03932
J. Am. Chem. Soc. 2016, 138, 8824−8833

Scheme 1. Summary of Electrochemistry, Crystallographic, and Morphological Changes of the Li_2MnO_3·$LiMO_2$ Electrode during Charge and Discharge

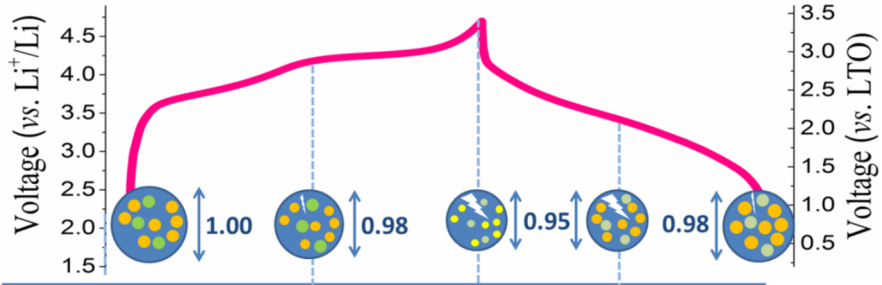

Crystallography and phase evolution				
Reaction type	$LiMO_2$ solid-solution	$LiMO_2$ 2-phase & Li_2MnO_3 oxygen evolution	$LiMO_2$ 2-phase & MnO_2 lithiation	$LiMO_2$ solid-solution & MnO_2 lithiation
$LiMO_2$ lattice parameter *a*	~1.3% reduction	0%	0%	~2.1% expansion
$LiMO_2$ lattice parameter *c*	~2.0% expansion	0%	0%	~2.0% reduction
$LiMO_2$ lattice vol. change	~0.4% reduction	0%	0%	~2.2% expansion
$LiMO_2$ d_{012}	~0.4% reduction	~0.6% reduction	~0.4% expansion	~1.3% expansion
Morphology				
Crack formation	Cracks develop	Cracks intensify	No change	Cracks partially heal
Change in particle vol.	~2% reduction	~3% reduction	0%	~3% expansion

significant volume change and corresponding to the most severe particle cracking.

Upon discharge to 3.6 V (vs Li^+/Li), the two-phase reaction of $LiMO_2$ is reversed, with this correlating to a nearly unchanged morphology and size of the composite particle under TXM observation. Importantly, the generated particle cracks began to heal during the subsequent lithiation step (below 3.6 V vs Li^+/Li), with this rehealing process being principally associated with the reversible solid-solution reaction of the $LiMO_2$ phase, which involves reduction of Ni^{4+} to Ni^{2+} (with ionic radii 0.48 and 0.69 Å, respectively) and Co^{4+} to Co^{3+} (with ionic radii 0.53 to 0.61 Å, respectively). The Li_2MnO_3·$LiMO_2$ particle under TXM observation expands by ~3% during this healing step, consistent with the ~2.2% volume expansion indicated by the NPD measurement for this process. Interestingly, the healing of the particle cracks does not occur during the two-phase reaction of the $LiMO_2$ phase on discharge, despite this being accompanied by the largest expansion in phase volume. During delithiation, the direction of the reduction in particle size during the $LiMO_2$ phase solid-solution reaction (Figure 7a) was significantly different to that for the two-phase reaction of the $LiMO_2$ phase (also involving oxygen evolution from Li_2MnO_3, Figure 7b), indicative of phase separation in the composite particle.

By dividing the multiphase positive electrode particle under TXM observation into quadrants (as shown by regions I–IV in Figure S9 in the EIS) the direction of particle size changes can be compared between charge and discharge processes. The solid-solution reaction of $LiMO_2$ on charging to 4.5 V (vs Li^+/Li) resulted in particle size reduction in quadrants I and II, with particle cracks appearing in quadrant II (Figure S9a). Size reduction during the following two-phase reaction of the $LiMO_2$ phase and the reaction releasing oxygen from the Li_2MnO_3 phase occurred in quadrants II and III, where the cracking in the particle intensified (Figure S9b). On discharge to 3.6 V, the particle size remained nearly unchanged (Figure S9c). On further discharge from 3.6 to 2.0 V (vs Li^+/Li) and during the solid-solution reaction of the $LiMO_2$ phase, healing of the particle cracks occurred, presumably triggered by expansion in this quadrant. Other significant particle-size changes during this period took place in quadrants I and IV (Figure S9d). Overall, with respect to the original particle at OCV, the first charge process resulted in a significant shrinkage in quadrants II and III (Figure S9e), compared with minor contraction in quadrants I and II following the whole first cycle (Figure S9f). Phase-border shifts such as these are thought to contribute to poor cycle life,[27] with the spinel $LiMn_2O_4$-like phase transformed following the evolution of oxygen by Li_2MnO_3 in the $Li(Li_{0.2}Mn_{0.54}Ni_{0.13}Co_{0.13})O_2$ layered–layered composite electrode known to consist of nanodomains.[29] Taken together, these results point to phase separation within the intergrown multiphase particle occurring in concert with phase lattice-size changes during extended cycling as the underlying reasons for capacity loss of this electrode.

■ CONCLUSIONS

Operando neutron powder diffraction and transmission X-ray microscopy were applied to characterize the structural and morphological evolution of the Li_2MnO_3·$LiMO_2$ (*M* = Li, Mn, Ni, Co) composite electrode, with the *operando* approach enabling this information to be directly correlated to electrochemical function. The unique combination of these *operando* methods revealed the underlying phase transformations and mechanisms that are responsible for the initiation and intensification of particle cracking that likely leads to pulverization and capacity fade in this electrode.

The electrode is composed of ~27 wt % ($C2/m$ space group) Li_2MnO_3 and ~73 wt % $LiMO_2$ ($R\bar{3}m$ space group), with this multiphase composite shown previously to occur as an intergrowth system.

DOI: 10.1021/jacs.6b03932
J. Am. Chem. Soc. 2016, 138, 8824–8833

The charge−discharge curves for the coin cell used in the TXM experiment with Li as the counter electrode and the pouch cell containing LTO used in the NPD study are near-identical, with the results of both able to be correlated by potential against Li. During the initial charge to 3.0 V vs LTO (4.55 V vs Li^+/Li), the $LiMO_2$ phase undergoes a solid-solution reaction involving a ∼0.4% reduction in crystal volume that was associated with the appearance of cracks in the electrode particle under observation in the TXM experiment. On further charge to 3.15 V vs LTO (4.7 V vs Li^+/Li) the $LiMO_2$ phase underwent a two-phase reaction that occurred alongside the irreversible evolution of oxygen from the Li_2MnO_3 phase. The two-phase reaction of the $LiMO_2$ phase involves the most substantial change in phase volume for any electrode phase during its entire working range (estimated at ∼4.4% between phases), and is correlated with the significant intensification of cracking in the electrode particle under TXM observation. Therefore, this work reveals that while it is the two-phase reaction of the $LiMO_2$ phase on charge that likely causes electrode particle pulverization leading to capacity loss, it is the solid-solution reaction of the $LiMO_2$ phase preceding this reaction that initiates particle cracking.

During discharge, both the two-phase and solid-solution reactions of the $LiMO_2$ phase are reversed, and the cracks in the electrode particle under TXM observation are healed by the corresponding expansion in phase volume. Interestingly, it is the volume expansion taking place only during the solid-solution, and not the two-phase, reaction that is associated with this crack healing, despite the $LiMO_2$ two-phase process having a substantially larger volume expansion than the solid-solution process of the $LiMO_2$ phase. The TXM images point to phase separation occurring during the two-phase reaction of the $LiMO_2$ phase as the reason for the limited recovery of the electrode during this process, as evidenced by strong anisotropy in electrode particle size changes occurring.

Overall, it is both the magnitude of the phase lattice change and phase separation that leads to capacity fade of the $Li_2MnO_3{\cdot}LiMO_2$ composite electrode, with this work suggesting that the minimization of phase separation is key to reducing capacity fade of this electrode.

■ ASSOCIATED CONTENT

Supporting Information

The Supporting Information is available free of charge on the ACS Publications website at DOI: 10.1021/jacs.6b03932.

Figures S1−S9 (PDF)

■ AUTHOR INFORMATION

Corresponding Authors

*vanessa.peterson@ansto.gov.au

*rsliu@ntu.edu.tw

Author Contributions

∇C. J. Chen and W. K. Pang contributed equally.

Notes

The authors declare no competing financial interest.

■ ACKNOWLEDGMENTS

The authors are grateful for the financial support of the Ministry of Science, Technology of Taiwan (Contract No. MOST 104-2113-M-002-012-MY3), the Ministry of Economic Affairs (103-EC-17-A-08-S1-183) and Academia Sinica (Contract No. AP-104-TP-A06) and to the staff members at the Australian Centre for Neutron Scattering at ANSTO for their operations support.

■ REFERENCES

(1) Blankenship, R. E.; Tiede, D. M.; Barber, J.; Brudvig, G. W.; Fleming, G.; Ghirardi, M.; Gunner, M. R.; Junge, W.; Kramer, D. M.; Melis, A.; Moore, T. A.; Moser, C. C.; Nocera, D. G.; Nozik, A. J.; Ort, D. R.; Parson, W. W.; Prince, R. C.; Sayre, R. T. *Science* **2011**, *332*, 805−809.

(2) U.S. Energy Information Administration (EIA). *Annual Energy Outlook 2015 with Projections to 2040*. http://www.eia.gov/forecasts/aeo/ (accessed March 25, 2016).

(3) Habisreutinger, S. N.; Schmidt-Mende, L.; Stolarczyk, J. K. *Angew. Chem., Int. Ed.* **2013**, *52*, 7372−7408.

(4) Quartarone, E.; Mustarelli, P. *Chem. Soc. Rev.* **2011**, *40*, 2525−2540.

(5) Peled, E.; Menachem, C.; Bar-Tow, D.; Melman, A. *J. Electrochem. Soc.* **1996**, *143*, L4−L7.

(6) Chan, C. K.; Peng, H.; Liu, G.; McIlwrath, K.; Zhang, X. F.; Huggins, R. A.; Cui, Y. *Nat. Nanotechnol.* **2008**, *3*, 31−35.

(7) Amatucci, G. G.; Tarascon, J. M.; Klein, L. C. *J. Electrochem. Soc.* **1996**, *143*, 1114−1123.

(8) Jo, M.; Hong, Y.-S.; Choo, J.; Cho, J. *J. Electrochem. Soc.* **2009**, *156*, A430−A434.

(9) Thackeray, M. M.; Kang, S.-H.; Johnson, C. S.; Vaughey, J. T.; Benedek, R.; Hackney, S. A. *J. Mater. Chem.* **2007**, *17*, 3112−3125.

(10) Liu, H.; Fell, C. R.; An, K.; Cai, L.; Meng, Y. S. *J. Power Sources* **2013**, *240*, 772−778.

(11) Tarascon, J. M.; Armand, M. *Nature* **2001**, *414*, 359−367.

(12) Goodenough, J. B.; Kim, Y. *Chem. Mater.* **2010**, *22*, 587−603.

(13) Johnson, C. S.; Kim, J. S.; Lefief, C.; Li, N.; Vaughey, J. T.; Thackeray, M. M. *Electrochem. Commun.* **2004**, *6*, 1085−1091.

(14) Zheng, J. M.; Zhang, Z. R.; Wu, X. B.; Dong, Z. X.; Zhu, Z.; Yang, Y. *J. Electrochem. Soc.* **2008**, *155*, A775−A782.

(15) Kang, S.-H.; Thackeray, M. M. *Electrochem. Commun.* **2009**, *11*, 748−751.

(16) Liu, J.; Wang, Q.; Reeja-Jayan, B.; Manthiram, A. *Electrochem. Commun.* **2010**, *12*, 750−753.

(17) Ito, A.; Li, D.; Sato, Y.; Arao, M.; Watanabe, M.; Hatano, M.; Horie, H.; Ohsawa, Y. *J. Power Sources* **2010**, *195*, 567−573.

(18) Zhang, H. Z.; Qiao, Q. Q.; Li, G. R.; Ye, S. H.; Gao, X. P. *J. Mater. Chem.* **2012**, *22*, 13104−13109.

(19) Ohzuku, T.; Nagayama, M.; Tsuji, K.; Ariyoshi, K. *J. Mater. Chem.* **2011**, *21*, 10179−10188.

(20) Gallagher, K. G.; Croy, J. R.; Balasubramanian, M.; Bettge, M.; Abraham, D. P.; Burrell, A. K.; Thackeray, M. M. *Electrochem. Commun.* **2013**, *33*, 96−98.

(21) Croy, J. R.; Gallagher, K. G.; Balasubramanian, M.; Chen, Z.; Ren, Y.; Kim, D.; Kang, S.-H.; Dees, D. W.; Thackeray, M. M. *J. Phys. Chem. C* **2013**, *117*, 6525−6536.

(22) Yu, H.; Ishikawa, R.; So, Y.-G.; Shibata, N.; Kudo, T.; Zhou, H.; Ikuhara, Y. *Angew. Chem.* **2013**, *125*, 6085−6089.

(23) Boulineau, A.; Croguennec, L.; Delmas, C.; Weill, F. *Chem. Mater.* **2009**, *21*, 4216−4222.

(24) Pang, W. K.; Alam, M.; Peterson, V. K.; Sharma, N. *J. Mater. Res.* **2015**, *30*, 373−380.

(25) Berg, H.; Rundlöv, H.; Thomas, J. O. *Solid State Ionics* **2001**, *144*, 65−69.

(26) Thackeray, M. M.; Johnson, P. J.; de Picciotto, L. A.; Bruce, P. G.; Goodenough, J. B. *Mater. Res. Bull.* **1984**, *19*, 179−187.

(27) Kraytsberg, A.; Ein-Eli, Y. *Adv. Energy Mater.* **2012**, *2*, 922−939.

(28) Johnson, C. S.; Li, N.; Lefief, C.; Vaughey, J. T.; Thackeray, M. M. *Chem. Mater.* **2008**, *20*, 6095−6106.

(29) Song, B.; Liu, Z.; Lai, M. O.; Lu, L. *Phys. Chem. Chem. Phys.* **2012**, *14*, 12875−12883.

(30) Mohanty, D.; Kalnaus, S.; Meisner, R. A.; Rhodes, K. J.; Li, J.; Payzant, E. A.; Wood, D. L., III; Daniel, C. *J. Power Sources* **2013**, *229*, 239−248.

DOI: 10.1021/jacs.6b03932
J. Am. Chem. Soc. 2016, 138, 8824−8833

(31) Shen, C.-H.; Huang, L.; Lin, Z.; Shen, S.-Y.; Wang, Q.; Su, H.; Fu, F.; Zheng, X.-M. *ACS Appl. Mater. Interfaces* **2014**, *6*, 13271−13279.
(32) Liu, H.; Chen, Y.; Hy, S.; An, K.; Venkatachalam, S.; Qian, D.; Zhang, M.; Meng, Y. S. *Adv. Energy Mater.* **2016**, *6*, 1502143.
(33) Liss, K.-D.; Hunter, B.; Hagen, M.; Noakes, T.; Kennedy, S. *Phys. B* **2006**, *385−386* (Part 2), 1010−1012.
(34) Toby, B. H.; Von Dreele, R. B. *J. Appl. Crystallogr.* **2013**, *46*, 544−549.
(35) Pang, W. K.; Peterson, V. K. *J. Appl. Crystallogr.* **2015**, *48*, 280−290.
(36) Studer, A. J.; Hagen, M. E.; Noakes, T. J. *Phys. B* **2006**, *385−386* (Part 2), 1013−1015.
(37) Rodríguez-Carvajal, J. *Phys. B* **1993**, *192*, 55−69.
(38) Roisnel, T.; Rodriguez-Carvajal, J. *Materials Science Forum, Proceedings of the Seventh European Powder Diffraction Conference (EPDIC 7)*; 2000; pp 118−123.
(39) Richard, D.; Ferrand, M.; Kearley, G. J. *J. Neutron Res.* **1996**, *4*, 33−39.
(40) Li, X.; Cai, W.; An, J.; Kim, S.; Nah, J.; Yang, D.; Piner, R.; Velamakanni, A.; Jung, I.; Tutuc, E.; Banerjee, S. K.; Colombo, L.; Ruoff, R. S. *Science* **2009**, *324*, 1312−1314.
(41) Chao, S.-C.; Yen, Y.-C.; Song, Y.-F.; Chen, Y.-M.; Wu, H.-C.; Wu, N.-L. *Electrochem. Commun.* **2010**, *12*, 234−237.
(42) Chao, S.-C.; Yen, Y.-C.; Song, Y.-F.; Sheu, H.-S.; Wu, H.-C.; Wu, N.-L. *J. Electrochem. Soc.* **2011**, *158*, A1335−A1339.
(43) Chao, S.-C.; Song, Y.-F.; Wang, C.-C.; Sheu, H.-S.; Wu, H.-C.; Wu, N.-L. *J. Phys. Chem. C* **2011**, *115*, 22040−22047.
(44) Jang, Y. I.; Huang, B.; Chiang, Y. M.; Sadoway, D. R. *Electrochem. Solid-State Lett.* **1998**, *1*, 13−16.
(45) Arico, A. S.; Bruce, P.; Scrosati, B.; Tarascon, J.-M.; van Schalkwijk, W. *Nat. Mater.* **2005**, *4*, 366−377.
(46) Johnson, C. S.; Li, N.; Lefief, C.; Thackeray, M. M. *Electrochem. Commun.* **2007**, *9*, 787−795.
(47) Chen, Y.; Xie, K.; Zheng, C.; Ma, Z.; Chen, Z. *ACS Appl. Mater. Interfaces* **2014**, *6*, 16888−16894.
(48) Hy, S.; Felix, F.; Rick, J.; Su, W.-N.; Hwang, B. J. *J. Am. Chem. Soc.* **2014**, *136*, 999−1007.
(49) Julien, C. M.; Mauger, A.; Zaghib, K.; Groult, H. *Inorganics* **2014**, *2*, 132−154.
(50) Dolotko, O.; Senyshyn, A.; Mühlbauer, M. J.; Nikolowski, K.; Ehrenberg, H. *J. Power Sources* **2014**, *255*, 197−203.
(51) Alam, M.; Hanley, T.; Pang, W. K.; Peterson, V. K.; Sharma, N. *Powder Diffr.* **2014**, *29*, S35−S39.
(52) Pang, W. K.; Kalluri, S.; Peterson, V. K.; Dou, S. X.; Guo, Z. *Phys. Chem. Chem. Phys.* **2014**, *16*, 25377−25385.
(53) Pang, W. K.; Sharma, N.; Peterson, V. K.; Shiu, J.-J.; Wu, S.-H. *J. Power Sources* **2014**, *246*, 464−472.
(54) Pang, W. K.; Peterson, V. K.; Sharma, N.; Shiu, J.-J.; Wu, S.-h. *Chem. Mater.* **2014**, *26*, 2318−2326.
(55) Pang, W. K.; Peterson, V. K.; Sharma, N.; Shiu, J.-J.; Wu, S.-h. *Powder Diffr.* **2014**, *29*, S59−S63.
(56) Chen-Wiegart, Y.-c. K.; Liu, Z.; Faber, K. T.; Barnett, S. A.; Wang, J. *Electrochem. Commun.* **2013**, *28*, 127−130.
(57) Liu, Z.; Scott Cronin, J.; Chen-Wiegart, Y.-c. K.; Wilson, J. R.; Yakal-Kremski, K. J.; Wang, J.; Faber, K. T.; Barnett, S. A. *J. Power Sources* **2013**, *227*, 267−274.
(58) Shin, Y.; Manthiram, A. *J. Electrochem. Soc.* **2004**, *151*, A204−A208.

DOI: 10.1021/jacs.6b03932
J. Am. Chem. Soc. 2016, 138, 8824−8833